ADVANCED OPTICAL MATERIALS
www.advopticalmat.de

Enhanced Performance of Gallium-Based Wide Bandgap Oxide Semiconductor Heterojunction Photodetector for Solar-Blind Optical Communication via Oxygen Vacancy Electrical Activity Modulation

Chao Wu, Tianli Zhao, Huaile He, Haizheng Hu, Zeng Liu, Shunli Wang, Fabi Zhang, Qinfeng Wang, Aiping Liu, Fengmin Wu,* and Daoyou Guo**

Gallium oxide (β-Ga_2O_3) is a prominent representative of the new generation of wide-bandgap semiconductors, boasting a bandgap of ≈4.9 eV. However, the growth process of β-Ga_2O_3 materials introduces unavoidable oxygen vacancies (Vo), leading to persistent photoconductivity (PPC), a phenomenon that severely hinders device performance. In this study, an innovative approach is successfully developed by introducing high p-orbital energy nitrogen (N). This leads to the formation of a hybridized state with O 2p orbitals in β-Ga_2O_3, resulting in the creation of GaON and suppressing the electrical activity of Vo. Through meticulous experimentation and advanced computational methods, a comprehensive and insightful explanation of the regulation and mechanism underlying this passivation process is offered. Moreover, *pn*-junction solar-blind photodetectors are engineered using hybridized GaON thin films with *p*-type CuPc. These photodetectors demonstrate exceptional characteristics, including ultra-low dark current (10^{-14} A), high photo-to-dark current ratio (10^6), and rapid decay speed (0.008 s) even at zero bias. Based on these advancements, a solar-blind ultraviolet communication system is designed, featuring straightforward and reliable encoding, easy implementation, and robust anti-interference capabilities.

1. Introduction

Solar-blind communication, operating within the wavelength range of 200–280 nm in the deep ultraviolet (DUV) spectrum, represents a cutting-edge technique that capitalizes on the utilization of ultraviolet radiation for signal transmission via the scattering and reflection phenomena involving airborne particles and aerosols.[1–3] Endowed with a plethora of distinctive attributes, this novel approach exhibits immense potential as a communication technology for future applications. Unlike conventional wireless communication, which necessitates a clear communication path between transmitters and receivers, solar-blind communication employing UV radiation effortlessly circumvents such hindrances through the mechanisms of scattering and reflection. Notably, the absorption of solar-blind radiation by ozone and oxygen in the atmosphere results in

C. Wu, T. Zhao, H. He, H. Hu, S. Wang, A. Liu, F. Wu, D. Guo
Department of Physics
Zhejiang Sci-Tech University
Hangzhou 310000, China
E-mail: slwang@zstu.edu.cn; wfm@zstu.edu.cn; dyguo@zstu.edu.cn

C. Wu, T. Zhao, H. He, H. Hu, A. Liu, F. Wu, D. Guo
Center for Optoelectronics Materials and Devices and Key Laboratory of Optical Field Manipulation of Zhejiang Province
Hangzhou 310018, China

Z. Liu
Innovation Center for Gallium Oxide Semiconductor (IC-GAO)
College of Integrated Circuit Science and Engineering
Nanjing University of Posts and Telecommunications
Nanjing 210023, China

S. Wang
Changshan Research Institute
Zhejiang Sci-Tech University
Changshan 324200, China

F. Zhang
Guangxi Key Laboratory of Precision Navigation Technology and Application
Guilin University of Electronic Technology
Guilin 541004, China

Q. Wang
Tiantong Holding Co., LTD
Haining 314400, China

The ORCID identification number(s) for the author(s) of this article can be found under https://doi.org/10.1002/adom.202302294

DOI: 10.1002/adom.202302294

the establishment of a communication channel characterized by low background noise in close proximity to the terrestrial surface. In the absence of radio interference, solar-blind communication emerges as a viable alternative to conventional wireless communication methodologies. Specifically designed for solar-blind optical communication, photodetectors possess specialized sensitivity to solar-blind light, ensuring efficient operation in challenging environments. Moreover, they boast desirable features such as low dark current and rapid response speed, further enhancing their performance and reliability. As a result, photodetectors stand as indispensable components within these communication systems, facilitating seamless and effective light-to-electrical signal conversion.[4,5] At present, commercially available silicon-based solar-blind photodetectors, while technologically mature, still encounter several challenges. These include reliance on filters, limited penetration depth for high-energy ultraviolet photons, and reduced responsivity in the solar-blind region. Ga_2O_3 stands out as the most promising candidate for solar-blind photodetector applications due to its ultra-wide bandgap (≈4.9 eV, corresponding to the solar-blind region), well-established material fabrication processes, and high stability.[6–10] Researchers are striving to establish Ga_2O_3-based *pn* heterojunctions,[11,12] *nn* heterojunctions,[13,14] phase junctions,[15,16] and Schottky junctions[17,18] to enhance the solar-blind response performance. However, during the material fabrication process, the unavoidable introduction of oxygen vacancy defects (Vo) leads to a substantial dark current (I_{dark}) in the detectors and triggers persistent photoconductivity (PPC), resulting in low detectivity and slow response speed.[19,20] Consequently, these detectors fall short of meeting the requirements for solar-blind communication applications. Therefore, there is a pressing need to develop methods that can effectively suppress vacancy-electrically-active effects and bolster photodetector performance.

Despite some experimental methods aimed at suppressing Vo in Ga_2O_3, an effective approach to fully shield their influence has not yet been found. In the past, the regulation of Vo concentration often relied on oxidation techniques, such as high-temperature annealing in an oxygen atmosphere and strong oxidizing agent treatment.[21–23] However, these methods only improved Vo on the surface and near-surface of Ga_2O_3 materials and had limited effects on controlling Vo within the bulk. Hybridization of band orbitals is an important approach to address the oxygen vacancy issue in oxide semiconductors. By introducing ions with high p orbital energy levels that couple with the O 2p orbitals of the oxide, it becomes possible to effectively shield impurity energy levels associated with oxygen vacancies and suppress their electrical activity. Kim et al. tackled this challenge ingeniously by introducing nitrogen into ZnO and capitalizing on the hybridization between N 2p and O 2p orbitals, as well as their interaction with metal d orbital electrons.[24,25] These modifications induced a fundamental change in the energy band structure near the valence band of ZnO, effectively mitigating the capture of charge carriers by Vo deep-level defects and thus suppressing the PPC effect in ZnO-based optoelectronic devices. In recent years, with the increasing interest in Ga_2O_3 research, some reports have emerged regarding its alloying with nitrogen anions.[26–30] However, the regulations governing Vo control and the underlying physical mechanisms are still not well understood. Additionally, the preparation of GaON continues to pose challenges, with current reported methods exhibiting limitations. Plasma-enhanced chemical vapor deposition (PECVD) stands out as a widely used thin film deposition technique, leveraging a reactive environment generated by plasma to facilitate chemical reactions and enable controlled film growth. This distinctive feature of PECVD enables the deposition of films with customized properties, making it especially well-suited for manufacturing advanced semiconductor devices with specific performance requirements.

Here, we performed a detailed characterization of Vo in Ga_2O_3 thin films using in situ etching X-ray photoelectron spectroscopy (XPS) and discussed the PPC effect in heterojunction photodetectors. We synthesized GaON alloy thin films using the PECVD method to suppress the electrical activity of internal oxygen vacancies. By adjusting the precursor ratios, we easily controlled the composition, bandgap, and Vo in Ga_2O_3. Through the use of well-established experimental and computational methods, we investigated the mechanism of GaON's ability to suppress oxygen vacancy electrical activity and studied its detailed electrical characteristics. In addition to that, we successfully engineered *pn* junction solar-blind photodetectors utilizing hybridized GaON thin films with p-type CuPc, showcasing exceptional characteristics such as ultra-low dark current (10^{-14} A), high photo-to-dark current ratio (10^6), and rapid decay speed (0.008 s) even at zero bias. These advancements served as the basis for designing a solar-blind ultraviolet communication system with user-friendly and reliable encoding, straightforward implementation, and robust anti-interference capabilities. Overall, our study's innovative technique effectively addresses the long-standing challenge of passivating oxygen vacancy impurity levels, establishing a strong groundwork for the application of gallium-based wide bandgap oxide semiconductor photodetectors in solar-blind communication systems and making a significant contribution to the advancement of semiconductor technology in optoelectronic devices.

2. Results and Discussion

This study showcases a Ga_2O_3-based heterojunction comprising n-type β-Ga_2O_3 and p-type CuPc as shown in **Figure 1a**. CuPc possesses captivating electrical and optical properties, rendering it highly sought after for utilization in a broad range of electronic and optoelectronic devices.[31–33] In our previous research, we employed a straightforward solution-processing approach to fabricate CuPc/β-Ga_2O_3 *pn* junction photodetectors, which demonstrated remarkable sensitivity.[34] Nevertheless, these photodetectors suffer from a drawback in their real-time response due to the PPC effect. As a result, the photocurrent typically takes a considerable amount of time to return to its initial value after the light source is turned off, rendering it unsuitable for optical communications. So far, extensive research has been conducted on the origin of the PPC effect in β-Ga_2O_3-based photodetectors.[35–37] Two primary mechanisms have been proposed to elucidate the dynamics of photocarriers under the PPC effect (Figure 1b). The first mechanism is associated with intrinsic defect-induced trap states, with the Vo in β-Ga_2O_3 being the main culprit introducing deep traps within the bandgap. Upon exposure to light, the deep neutral Vo states are ionized into shallow donor states Vo^{2+}, liberating two electrons and leading to an augmented photoconductivity. However, the neutralization of

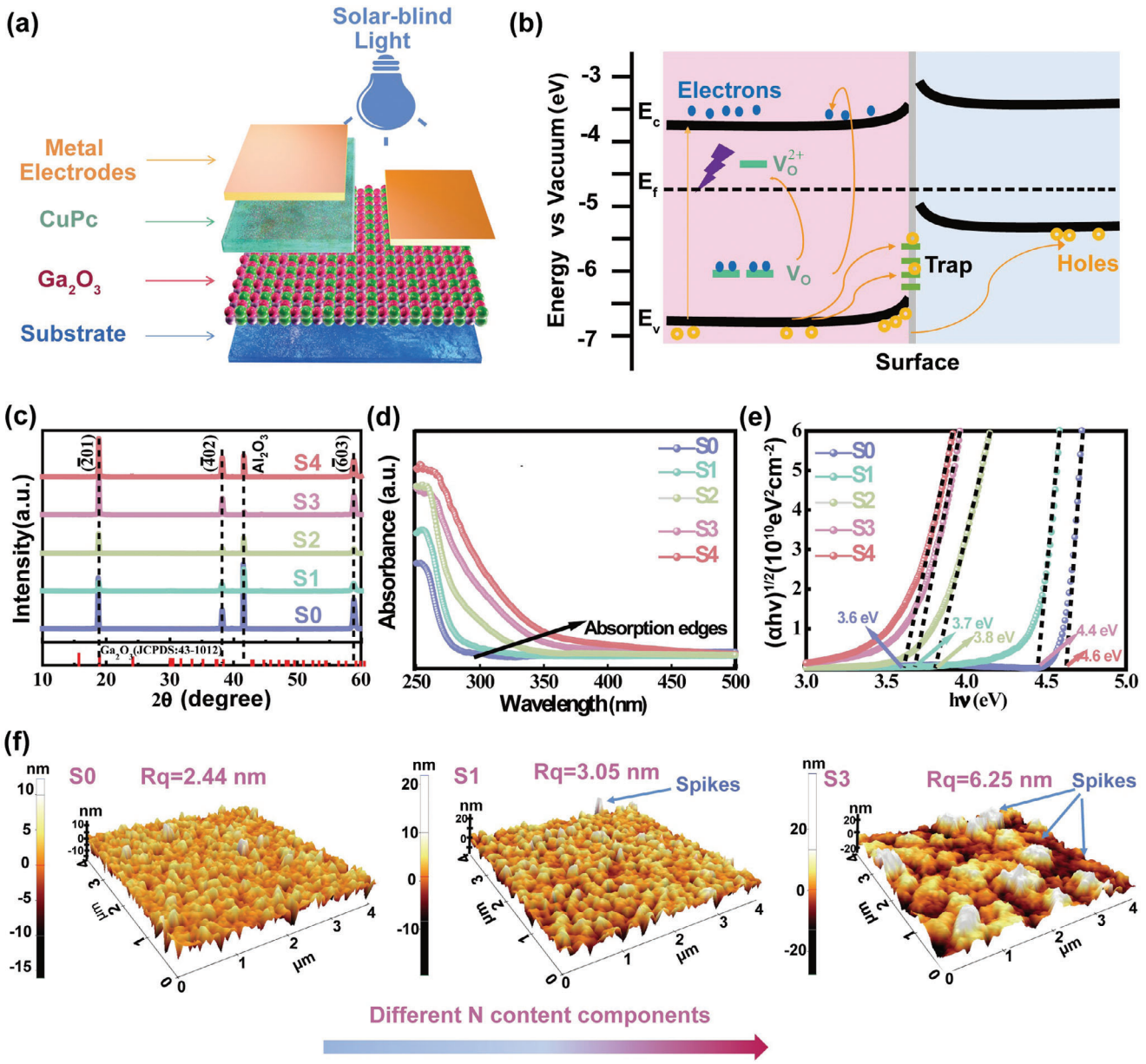

Figure 1. a) Schematic diagram of the heterojunction photodetector. b) Schematic diagram of the PPC effect. c) XRD results of S0-S4 films grown by PECVD. d,e) UV–vis spectra and bandgap of S0–S4 films grown by PECVD. f) AFM-measured surface profiles of the S0, S1, and S3 samples (scanning area is 4 × 4 μm^2).

the Vo^{2+} states necessitate overcoming an energy barrier caused by significant lattice relaxation. The second mechanism emphasizes the role of surface trap states. In metal oxides like β-Ga_2O_3, the surface harbors a high density of trap states that facilitate the separation of photogenerated electron-hole pairs. As a consequence, trapped holes accumulate on the surface, contributing to the observed PPC effect. By comprehending and addressing these underlying mechanisms, researchers can enhance their understanding of photoconductive behavior and devise strategies to optimize the performance of β-Ga_2O_3-based photodetector.[38] Here, we mainly use anionic alloy engineering to inhibit the internal oxygen vacancy electrical activity. We employed PECVD to synthesize GaON alloy thin films to hybridization between nitrogen 2p and oxygen 2p orbitals and of mitigating the electrical activity of internal oxygen vacancies. By carefully manipulating the growth conditions, we successfully minimized the presence and impact of Vo within the material. The X-ray diffraction (XRD) spectra of the samples grown by PECVD are displayed in Figure 1c. The nitrogen flux was systematically varied from 0 to 20, 50, 100, and 150 SCCM, corresponding to the samples designated as S0, S1, S2, S3, and S4, respectively. All the samples exhibit three prominent peaks at 18.8°, 38.2°, and 58.9°, which can be attributed to the ($\bar{2}$01), ($\bar{4}$02), and ($\bar{6}$03) crystallographic planes of β-Ga_2O_3.[39,40] This indicates that GaON retains the β phase

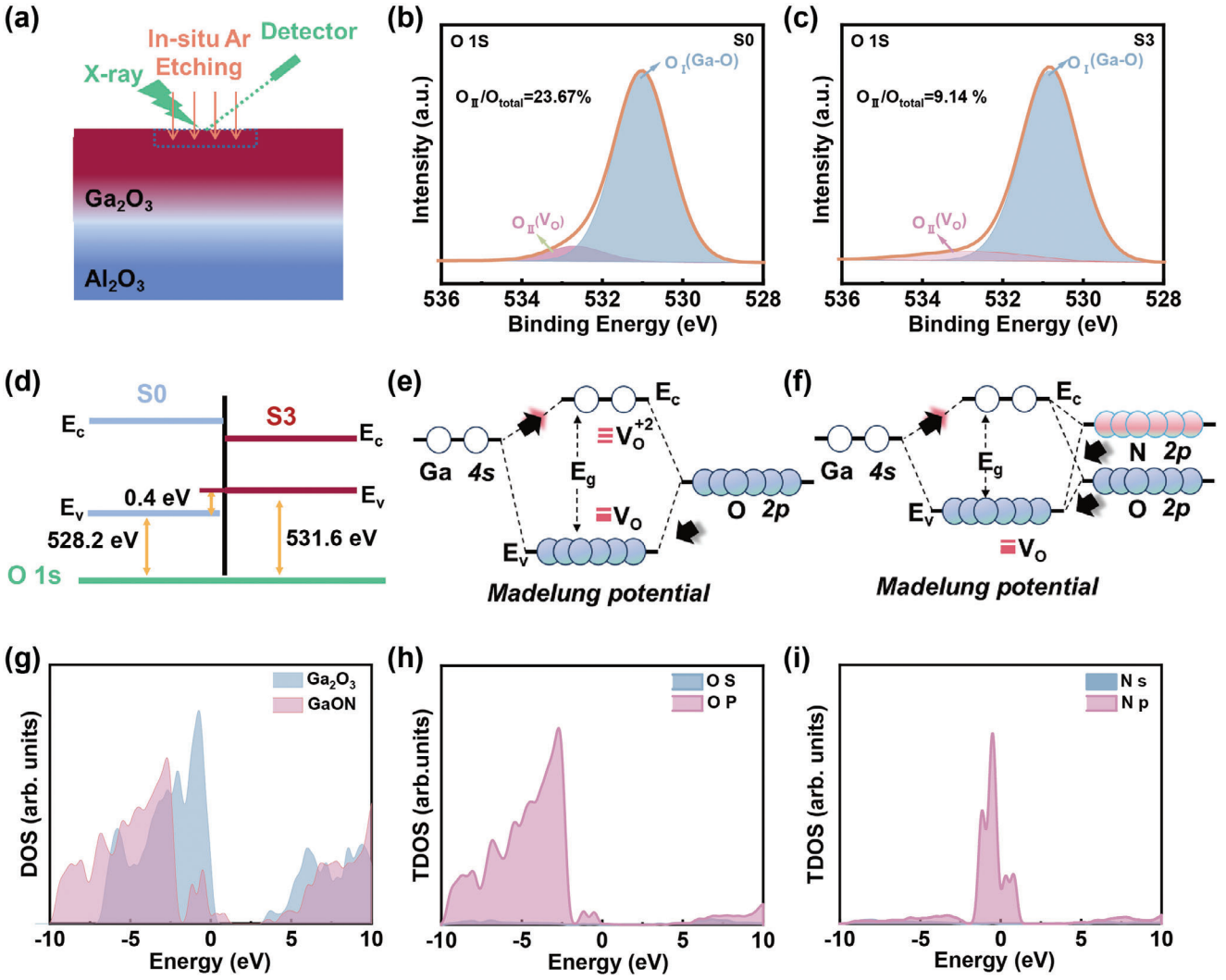

Figure 2. a) Illustration of in-situ etching XPS measurement. b,c) O 1s XPS spectrum of sample S0 and S3, respectively. d) Band structure of S0 and S3. e,f) Schematic diagrams of bandgap formation mechanisms in S1 and S3. g–i) Density of states (DOS) of GaON and Ga_2O_3 calculated using DFT.

structure even after nitrogen incorporation through the PECVD process. With the increasing incorporation of nitrogen, the diffraction peak of the $(\bar{2}01)$ plane undergoes a subtle blue shift, and the surface lattice expands with the integration of nitrogen. Notably, as the nitrogen flux increases from 0 to 100 SCCM, a considerable red shift in the absorption edge is observed, as shown in Figure 1d. The optical bandgap can be calculated from the extrapolation of the Tauc equation for allowed direct transitions:[41,42]

$$(\alpha h\upsilon)^2 = B \cdot (h\upsilon - E_g) \quad (1)$$

where B is a constant, α is the absorption coefficient, h is Planck's constant, n is the incident photon frequency, and E_g is the optical bandgap. The bandgap of the five samples lies between 4.9 and 3.4 eV, indicating a range of optical properties resulting from the varying nitrogen incorporation (Figure 1e). In Figure 1f, we can observe the representative 3D atomic force microscopy (AFM) images of samples S0, S1, and S3. The electron affinity difference between oxygen and nitrogen plays a significant role in determining the bond strength between gallium and these elements.[43] As a consequence, the bond between gallium and oxygen is more energetically favorable and thermodynamically stable than the bond between gallium and nitrogen, leading to lower thermal stability of GaON. Initially, the Ga_2O_3 sample exhibited a high-quality surface with a low surface roughness (R_q) of 2.44 nm. However, upon the introduction of nitrogen, the thin film's surface displayed the formation of spike-like structures, indicating noticeable changes in the film's morphology. The characteristics of samples S0 through S4 were encapsulated in Table S1, Supporting Information.

To further investigate the changes in Vo defects within the samples, XPS measurements were performed on different samples using in situ Ar^+ sputtering, as depicted in **Figure 2a**. Figure 2b,c displays the distribution of the O 1s peak after etching 40 nm of material from the S0 and S3 samples, revealing two distinct components (I and II).[44,45] After the introduction of nitrogen, the II peak, typically associated with Vo defects, experienced a significant reduction, indicating a substantial decrease

in the Vo defects concentration. To further substantiate the XPS findings, we employed solid-state laser Raman spectroscopy with a wavelength of 532 nm (Figure S1, Supporting Information). The Raman-active modes of β-Ga_2O_3 are conventionally categorized into three frequency ranges: the low-frequency range below 200 cm^{-1}, corresponding to the liberation and translation of tetrahedron–octahedron chains; the frequency range between 200 and 500 cm^{-1}, linked to the deformation of GaO_6 octahedra; and the high-frequency range above 500 cm^{-1}, attributed to the stretching and bending of GaO_4 tetrahedra. Studies have indicated that purely octahedral vibrations are exclusively generated by Ga translations, whereas tetrahedral vibrations arise from the movement of oxygen atoms. The intensity of Raman modes at 199.8 and 420.5 cm^{-1} correlates with oxygen vacancy defects. With an increasing number of oxygen vacancies, a heightened likelihood of Ga release and translation is observed, resulting in elevated intensities of the Raman peaks at 199.8 and 420.5 cm^{-1}. Upon the introduction of nitrogen, S1 and S3 display lower Raman peak intensities at 199.8 and 420.5 cm^{-1} compared to S0, indicating a reduction in oxygen vacancies. This observation aligns seamlessly with XPS results. Photoluminescence measurements were conducted on films deposited using different N/O flow rates to investigate their oxygen vacancy defects. Figure S2, Supporting Information illustrates the emission of the blue band photoluminescence peak at 432 and 487 nm, which could be attributed to the recombination of a trapped hole in an acceptor with a trapped electron in a donor, where the acceptor originates from O_2 vacancies in the GaON thin films. The photoluminescence intensity of the GaON thin films with high N content (S1, S2, and S3) was considerably lower than that of the films without N content (S0). This disparity may be attributed to the presence of oxygen vacancy density resulting from N incorporation. In order to gain deeper insights into the underlying mechanism of Vo changes, understanding the band alignment is of utmost importance. By comparing the XPS spectra of the valence band (VB) levels (Figure S3, Supporting Information), it becomes possible to determine the offset of the valence band maximum (VBM) between GaON (S3) and Ga_2O_3 (S0). As depicted in Figure 2d, with the O 1s core level as a reference, the valence band maximum (VBM) offset is measured to be 0.4 eV, signifying that the VBM of the GaON is higher compared to Ga_2O_3. With the introduction of nitrogen, the Ga_2O_3 material experiences significant changes in its band structure. The hybridization of Ga 3d and O 2p orbitals, along with the repulsive force of the N 2p orbitals, causes the valence band maximum (VBM) to shift upward and leads to a reduction in the bandgap of GaON. Moreover, the hybridization of N 2p and O 2p orbitals at the VBM effectively screens or deactivates the energy level of the neutral oxygen vacancy, which closely aligns with the VBM (Figure 2e,f). To further understand the impact of nitrogen incorporation on the band structure of β-Ga_2O_3, we performed computational analysis on the differences in density of states (DOS). The DOS reveals that the valence band of β-Ga_2O_3 is mainly composed of O 2p states (Figure 2g–i). However, when nitrogen atoms replace oxygen atoms and form GaON in β-Ga_2O_3, new VBM states are formed through the hybridization of N 2p and O 2p states. Due to the higher energy level of N 2p states, the new VBM is significantly elevated, which is consistent with our experimental results.

In order to investigate the effects of oxygen vacancy electrical activity modulation on the photodetection performance, *pn* junction photodetectors based on CuPc and gallium-based wide bandgap oxide semiconductor films were fabricated and studied systematically. The photodetectors labeled as S0, S1, and S3 refer to the photodetectors fabricated using thin films of S0, S1, and S3, respectively. The typical *I–V* characteristics of S0, S1, and S3 samples are shown in **Figure 3**a–c. Under dark conditions, the dark current of different samples exhibits significant variations, while the photocurrent remains almost unchanged under solar-blind UV illumination. The S0 sample shows a high leakage current, which is associated with the abundance of Vo within the β-Ga_2O_3 film. However, as the amount of nitrogen in the sample increases, the dark current (I_{dark}) decreases. The S3 device exhibits 10^2 times lower I_{dark} (10^{-11} A at 5 V) than that of the S0 device. Furthermore, the I_{dark} of the S3 device at 0 V remains at an extremely low level of about 10^{14} A. This low I_{dark} can be attributed to the reduction in defect concentration. The combination of high photocurrent (I_{photo}) and low I_{dark} results in an impressive photo-to-dark current ratio (PDCR) in the device. Notably, sample S3 exhibits an exceptionally high PDCR of 2.7×10^6 at 0 V bias. However, upon introduction of N_2 with a flux of 150 sccm (S4), the dark current of the sample actually increases (10^{-9} A at 5 V). This is because the introduction of excessive nitrogen leads to other defects (Figures S4 and S5, Supporting Information). To assess the impact of anion engineering on the repeatability and response speed of the photodetector, we conducted time-dependent photoresponse characterization. By subjecting the devices to periodic on/off light switching, we repetitively stimulated the currents of each device (at 0 V, as shown in Figure 3d–f, and at 10 V, as shown in Figure S6, Supporting Information) without any noticeable degradation during the investigated cycles. This observation emphasizes the stable and reliable performance of the devices under such repetitive photoactivation, making them highly promising for practical applications. However, in the case of the S0 photodetector, a prolonged tail is observed during the decay process, indicating a PPC effect. This effect is linked to the abundance of Vo defects in the S0 film, leading to significant trapping/detrapping processes of charge carriers and prolonging the device recovery time before responding to the next stimulus. We employed an exponential function to fit and calculate the response time. The results reveal that the decay time of S0 is significantly longer than 0.21 s, while the S1 and S3 devices exhibit decay times of 0.01 and 0.008 s, respectively (Figure 3g–i). The swift response speed of the S3 photodetector can be attributed to the suppression of deep-level traps associated with Vo. From the spectral response characteristics depicted in Figure 3j–l, it is evident that all devices exhibit remarkable sensitivity in the solar-blind region. To assess the photodetector quantitively, responsivity (*R*), and detectivity (*D*) is introduced. As shown in Figures S7 and S8, Supporting Information, under a 100 μW cm^{-2} 254 nm light, the largest *R* values of S0 and S3 photodetector reached 0.61 and 0.79 mA W^{-1}, respectively. The largest *D* values of S0 and S3 photodetector reached 0.35×10^{12} and 1.41×10^{13} Jones, respectively. Based on the comprehensive analysis, the photodetector developed in this study showcases outstanding performance in multiple aspects. Particularly, it boasts an ultra-low dark current, high detectivity, and rapid response speed, making it a truly exceptional device (**Table 1**).

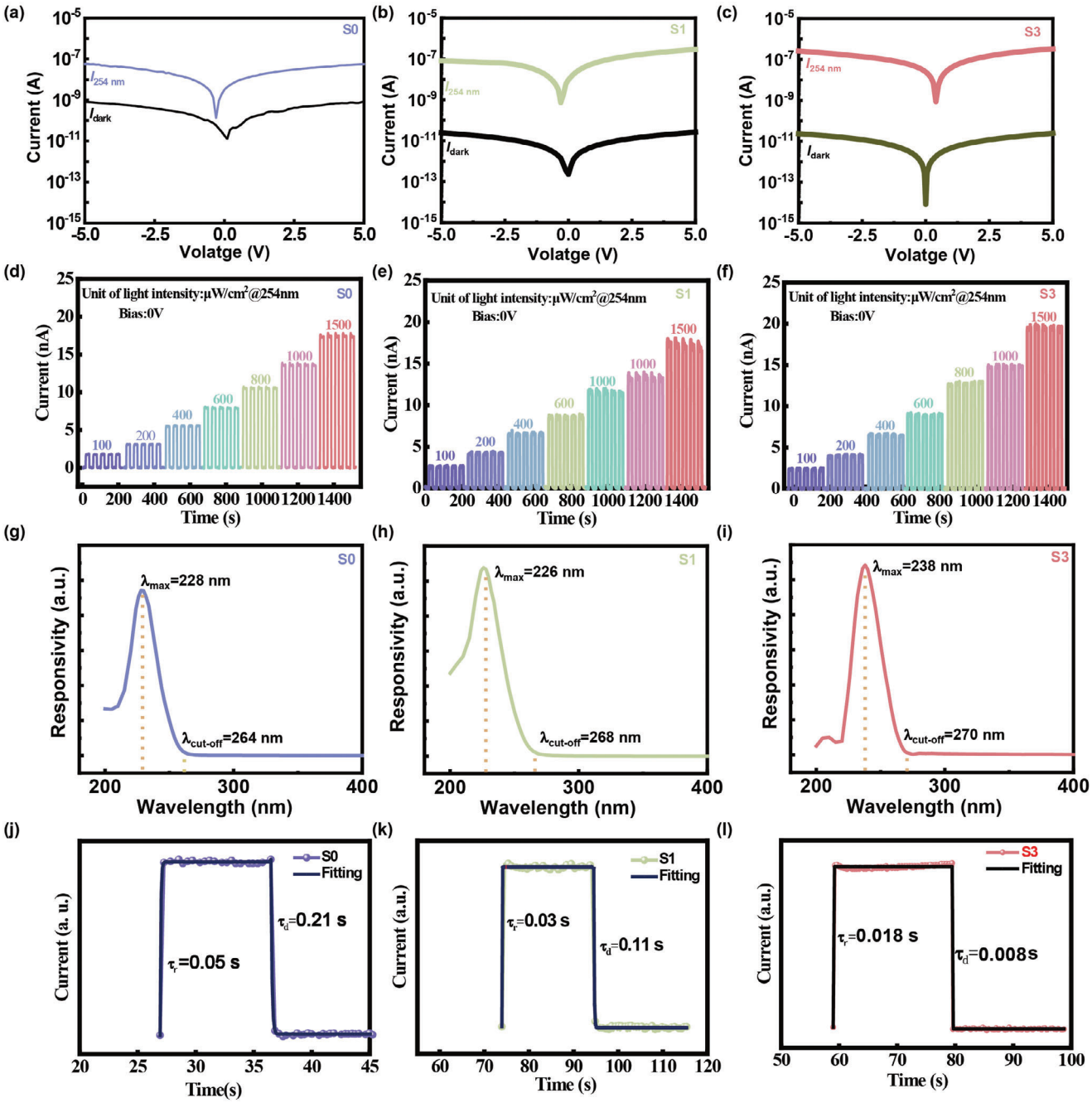

Figure 3. a–c) Log scale *I–V* curves of the S0, S1, and S3 photodetectors measured in the dark and under 254 nm UV illumination, respectively. d–f) The *I–t* curves of S0, S1, and S3 photodetectors measured at 0 V bias, respectively. g–i) The normalized spectral responsivity of S0, S1, and S3 photodetectors measured at 0 V bias, respectively. j–l) Response speed of S0, S1, and S3 photodetectors measured at 0 V bias, respectively.

Figure 4 illustrates the carrier transport mechanism in an S3 photodetector under different bias conditions using energy band diagrams. Figure 4a shows the energy band diagram before the formation of the heterojunction. When GaON and CuPc come into contact, carrier diffusion generates an inherent electric field, leading to the formation of a potential barrier that restricts the diffusion of electrons and holes, as depicted in Figure 4b. Under forward bias, the applied electric field reduces the potential barrier between GaON and CuPc by suppressing the inherent electric field. This facilitates the movement of electrons in GaON and holes in CuPc, allowing them to overcome the potential barrier Figure 4c. Conversely, under reverse bias (Figure 4d), minority carriers are driven by the external electric field, resulting in a small negative current. Under short-wavelength light, photogenerated electron-hole pairs near the GaON/CuPc depletion layer are separated by the built-in electric field and efficiently collected at the electrode at zero bias (Figure 4e). Nevertheless, electron–hole pairs separated under forward bias and reverse bias

Table 1. The parameters comparison of heterojunction photodetectors based on Ga_2O_3 from previous works and this work at zero bias.

Junction	I_{dark} [A]	PDCR	τ_d [s]	R [mA W^{-1}]	D [Jones]	Ref.
Ga_2O_3/ZnO	–	127	0.27	0.76	–	[46]
α/γ- Ga_2O_3	10^{-9}	127	1.63	0.26	2.8×10^9	[47]
Ga_2O_3/NiO	10^{-9}	122	3.65	0.05	5.5×10^9	[48]
Ga_2O_3/Diamond	10^{-9}	31	–	0.2	6.9×10^9	[49]
Ga_2O_3/CuI	10^{-12}	10^3	0.028	8.46	7.7×10^{11}	[50]
Ga_2O_3/MoS_2	10^{-12}	670	–	2.05	1.2×10^{11}	[51]
Ga_2O_3/PEDOT	10^{-13}	10^4	0.003	2.6	2.2×10^{13}	[52]
α/γ- Ga_2O_3	10^{-9}	51	0.1	0.17	–	[53]
Ga_2O_3/CuPC	10^{-12}	10^4	0.21	0.61	0.3×10^{12}	This work
GaON/CuPC	10^{-14}	10^6	0.008	0.79	1.4×10^{13}	This work

are shown in Figure 4f,g, respectively. These insights shed light on the intricate behavior of the photodetector under various bias conditions, providing a deeper understanding of its operating principles. This knowledge can facilitate the optimization of the photodetector's performance for specific applications.

Finally, we propose a streamlined framework for a solar-blind ultraviolet communication system, consisting of a transmitter, atmospheric channel, and receiver. At the transmitter, the original information is sent from the serial port to the Field Programmable Gate Array (FPGA) board, where it undergoes modulation and encoding by multiplying it with the carrier signal. This modulated signal is then output through the pins of the FPGA board, controlling the on and off states of the 254 nm ultraviolet LED. After traveling a certain distance, the information reaches the receiver through the atmospheric channel. At the receiver, the GaON/CuPc heterojunction photodetector serves as the light receiver, converting the optical signal into an analog pulse. Utilizing internal algorithms within the detector, the analog signal is directly transformed into a digital signal. These digital signals undergo various digital processing steps, such as filtering, symbol synchronization, and decision-making. Subsequently, they are sent via the serial port to a personal computer at the receiving end, thereby completing the information communication process, as illustrated in **Figure 5**a. When the 254 nm LED light emits an optical pulse, it represents signal 1, and the detector registers a higher light intensity. On the other hand, when the LED light does not emit any optical pulse, it represents signal 0, and the photodetector detects no light intensity. By setting the size of window, we can continuously monitor the real-time light intensity (with each new light intensity value detected, it enters the window at the end, displacing the oldest value in a cyclic manner). We then compute the threshold by calculating the weighted average of all the light intensity values within the window. Comparing the light intensity values at each moment within the window with the threshold allows us to determine the binary information, which is then stored in matrix, facilitating signal analog-to-digital conversion. The flowchart outlining the designed binary threshold algorithm is presented in Table S2, Supporting Information. To assess the algorithm's performance, we conducted an alignment of the detector with the horizontal position of the ultraviolet LED,

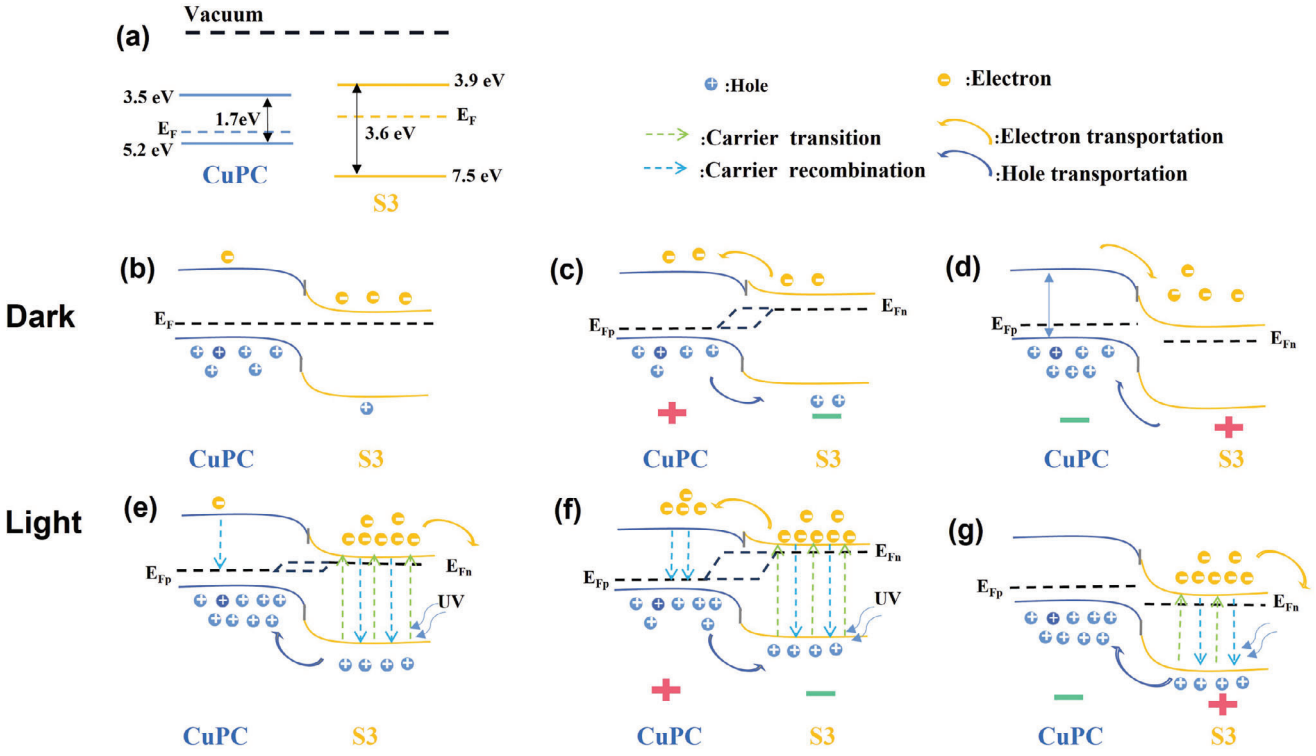

Figure 4. Schematic energy band diagrams of the S3 heterojunction. a) Before contact. b–d) Dark conditions (after contact) under 0 V bias, forward bias and reverse bias, respectively. e–g) UV illumination (after contact) under 0 V bias, forward bias, and reverse bias, respectively.

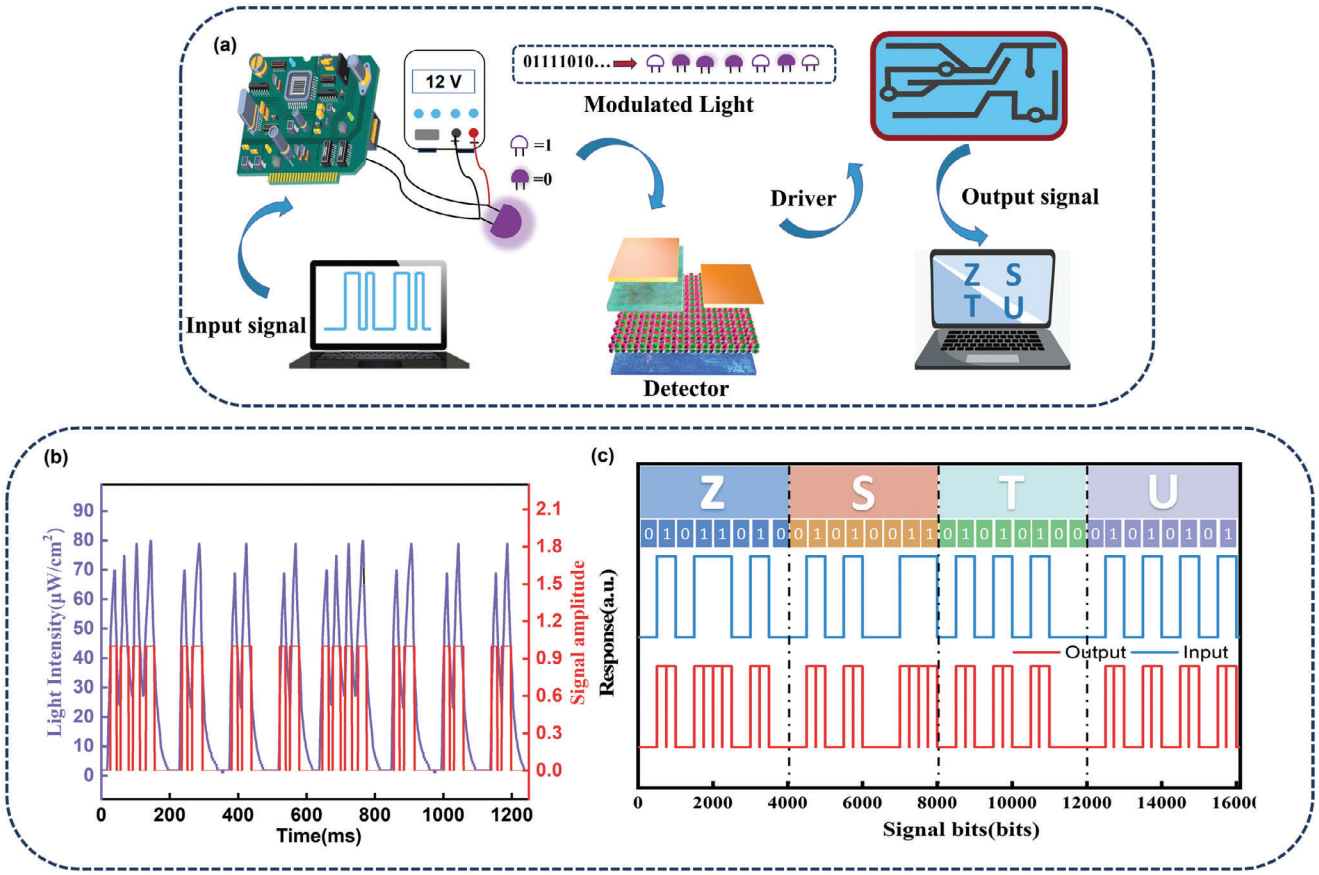

Figure 5. a) Schematic diagram of the solar-blind optical communication system. b) Received signal waveform diagram. c) The decode procedure of the photodetector used in optical communication according to ZSTU ASCII codes.

resulting in the data signal waveform depicted in Figure 5b. The purple curve represents the light intensity signal received by the detector, while the red curve represents the binary signal after undergoing algorithmic processing. Through the application of the binary threshold algorithm, the previously complex light intensity signal is efficiently converted into a readily manageable binary signal. By cross-referencing an ASCII to binary code conversion table, we determined that the binary codes for ZSTU are respectively represented as 0111_1010, 0111_0011, 0111_0100, 0111_0101. After undergoing meticulous demodulation processing, the system yields the precise baseband signal, as depicted in Figure 5c. As a consequence, it holds vast potential for extensive applications in diverse domains, encompassing military operations, non-line-of-sight communications, and other prospective fields.

3. Conclusion

In this work, we employed PECVD to synthesize GaON alloy thin films to hybridization between nitrogen 2p and oxygen 2p orbitals and of mitigating the electrical activity of internal oxygen vacancies. By carefully manipulating the growth conditions, we successfully minimized the presence and impact of oxygen vacancies within the material. XPS measurement and DFT calculation results shows that upon the introduction of nitrogen, the hybridization of Ga 3d and O 2p orbitals, along with the repulsive force of the N 2p orbitals, causes the VBM to shift upward and reduces the bandgap of the GaON material. Simultaneously, the energy level of the neutral oxygen vacancy, which closely aligns with the VBM, gets effectively screened or deactivated through the hybridization of N 2p and O 2p orbitals at the VBM. Owing to the suppression of PPC effect, the GaON/CuPc heterojunction-based photodetectors demonstrate low dark current, high photo-to-dark current ratio, and rapid decay speed. This significant advancement contributes to the progress of semiconductor technology in optoelectronic devices and offers promising opportunities for further advancements in the field.

4. Experimental Section

Film Fabrication and Characterization: Ga_2O_3 and GaON films were deposited on c-Al_2O_3 substrates using a PECVD system (Model: BTF-1200C-PECVD-500A, purchased from Anhui BEQ Equipment Technology Co., Ltd.). The c-Al_2O_3 substrate wafers were initially cleaned with acetone, ethanol, and deionized water to remove organic contaminants. The sources for N, O, and Ga were N_2, O_2, and high-purity metal Ga, respectively. The deposition process was carried out under controlled conditions, with a constant RF power of 200 W, an argon flux of 80 SCCM, an oxygen flux of 5 SCCM, and a growth temperature of 850 °C. To investigate the influence of N_2 flux on film properties, the N_2 flux was systematically varied

from 0 to 20, 50, 100, and150 SCCM, corresponding to the samples designated as S0, S1, S2, S3, and S4, respectively. X-ray diffraction (XRD) and X-ray photoelectron spectroscopy (XPS) measurements were conducted using D8 Discover and K-Alpha instruments, respectively. To understand the bonding conditions of the as-grown films, XPS measurements were performed on different samples with varying durations of in-situ Ar^+ sputtering. Absorption spectra were acquired using a UV–vis spectrophotometer (Hitachi U-3900UV). The morphology of the films was characterized using an atomic force microscope (AFM, XE-100E).

Device Fabrication: In the uncovered regions of the S0, S1, and S3 sample films, the spin-coating technique was employed to fabricate nanoscale-thick *pn* junctions using *p*-type CuPc. The CuPc solution concentration was set at 10 mg mL^{-1}, and the spin-coated films were carefully dried at a temperature of 100 °C. Subsequently, Ti/Au test electrodes were meticulously formed on the S0, S1, and S3 samples using magnetron sputtering, while Au test electrodes were skillfully prepared on the CuPc film. Rigorous measurements were carried out using KEITHLEY 4200, 2400, and 6487 for *I–V* and *I–t* characteristics measurements. Additionally, a spectral measurement system was employed to conduct wavelength-dependent photoresponse tests.

Development of a Solar-Blind Communication System: The transmitting end of the system mainly consisted of a transmitting terminal personal computer (PC), FPGA, driver circuit, and deep UV LED light source. At the transmitting end, the raw information was sent from the TX-PC to the FPGA board through the serial port and was multiplied with the carrier signal to generate the modulated encoded signal on the FPGA board. This signal was output through the pins of the FPGA board to the driver circuit, which controls the on–off state of the 254 nm ultraviolet LED light. The electrical signal was then converted into an optical signal and transmitted into the free atmosphere through the ultraviolet LED light. The main chip used in the driver circuit of the transmitting end was the AD8001AN operational amplifier. The XILINX company's ARTIX-7 series XC7A100T chip development board was used to implement the system's digital signal processing. To test the performance of the modulation module, data transmission between the transmitting end PC and the FPGA board was achieved through a USB data cable. An oscilloscope was used to test the waveform of the output signal from the FPGA at the transmitting end. After powering up the FPGA development board, the transmitting end code was downloaded to the board via the JTAG cable, and the raw data was sent using the serial debugging assistant. The serial port parameters of the computer were set as follows: baud rate is 115 200 B s^{-1}, no parity bit, data bits were 8 bits, and stop bits were 1 bit.

Supporting Information

Supporting Information is available from the Wiley Online Library or from the author.

Acknowledgements

This work was supported by the National Natural Science Foundation of China (No. 62274148, 62374147, 62304205), Joint Funds of the National Natural Science Foundation of China (No. U23A20349), Science Foundation of Zhejiang Sci-Tech University (No. 22062337-Y, 20062224-Y, 22062291-Y), Changshan Research Institute of Zhejiang Sci-Tech University, and Guangxi Key Laboratory of Precision Navigation Technology and Application (Guilin University of Electronic Technology, Grant no. DH202229).

Conflict of Interest

The authors declare no conflict of interest.

Data Availability Statement

The data that support the findings of this study are available on request from the corresponding author. The data are not publicly available due to privacy or ethical restrictions.

Keywords

alloy engineering, gallium oxide, oxygen vacancy regulation, solar-blind communication system, solar-blind photodetector

Received: September 17, 2023
Revised: December 11, 2023
Published online: January 15, 2024

[1] S. Fang, L. Li, D. Wang, W. Chen, Y. Kang, W. Wang, X. Liu, Y. Luo, H. Yu, H. Zhang, M. H. Memon, W. Hu, J.-H. He, C. Gong, C. Zuo, S. Liu, H. Sun, *Adv. Funct. Mater.* **2023**, *33*, 2214408.
[2] N. Alwadai, S. Mitra, M. N. Hedhili, H. Alamoudi, B. Xin, N. Alaal, I. S. Roqan, *ACS Appl. Mater. Interfaces* **2021**, *13*, 33335.
[3] S. Mitra, Y. Pak, N. Alaal, M. N. Hedhili, D. R. Almalawi, N. Alwadai, K. Loganathan, Y. Kumarasan, N. Lim, G. Y. Jung, I. S. Roqan, *Adv. Opt. Mater.* **2019**, *7*, 1900801.
[4] H. Alamoudi, B. Xin, S. Mitra, M. N. Hedhili, S. Venkatesh, D. Almalawi, N. Alwadai, Z. Alharbi, A. Subahi, I. S. Roqan, *Appl. Phys. Lett.* **2022**, *120*, 122102.
[5] N. Alwadai, Z. Alharbi, F. Alreshidi, S. Mitra, B. Xin, H. Alamoudi, K. Upadhyaya, M. N. Hedhili, I. S. Roqan, *ACS Appl. Mater. Interfaces* **2023**, *15*, 12127.
[6] D. H. Wang, X. Liu, Y. Kang, X. N. Wang, Y. P. Wu, S. Fang, H. B. Yu, M. H. Memon, H. C. Zhang, W. Hu, Z. T. Mi, L. Fu, H. D. Sun, S. B. Long, *Nat. Electron.* **2021**, *4*, 645.
[7] D. Wang, W. Wu, S. Fang, Y. Kang, X. Wang, W. Hu, H. Yu, H. Zhang, X. Liu, Y. Luo, J.-H. He, L. Fu, S. Long, S. Liu, H. Sun, *Light Sci. Appl.* **2022**, *11*, 227.
[8] X. Hou, X. Zhao, Y. Zhang, Z. Zhang, Y. Liu, Y. Qin, P. Tan, C. Chen, S. Yu, M. Ding, G. Xu, Q. Hu, S. Long, *Adv. Mater.* **2021**, *34*, 2106923.
[9] S. J. Pearton, J. Yang, P. H. Cary, F. Ren, J. Kim, M. J. Tadjer, M. A. Mastro, *Appl. Phys. Rev.* **2018**, *5*, 011301.
[10] Y. Hao, *J. Semicond.* **2019**, *40*, 010301.
[11] Y. Han, Y. Wang, S. Fu, J. Ma, H. Xu, B. Li, Y. Liu, *Small* **2023**, *19*, 2206664.
[12] W. Choi, J. Ahn, K.-T. Kim, H.-J. Jin, S. Hong, D. K. Hwang, S. Im, *Adv. Mater.* **2021**, *33*, 2103079.
[13] T. He, X. Zhang, X. Ding, C. Sun, Y. Zhao, Q. Yu, J. Ning, R. Wang, G. Yu, S. Lu, K. Zhang, X. Zhang, B. Zhang, *Adv. Opt. Mater.* **2019**, *7*, 1801563.
[14] C. Wu, F. Wu, L. Deng, S. Li, S. Wang, L. Cheng, A. Liu, J. Wang, W. Tang, D. Guo, *Vacuum* **2022**, *201*, 111064.
[15] Q. Li, B.-D. Du, J.-Y. Gao, J. Liu, *Appl. Phys. Rev.* **2023**, *10*, 011402.
[16] R. Zhu, H. L. Liang, H. Bai, T. Zhu, Z. X. Mei, *Appl. Mater. Today* **2022**, *29*, 101556.
[17] F. Therrien, A. Zakutayev, V. Stevanovic, *Phys. Rev. Appl.* **2021**, *16*, 064064.
[18] T. Harada, S. Ito, A. Tsukazaki, *Sci. Adv.* **2019**, *5*, eaax5733.
[19] C. Zhou, K. Liu, X. Chen, J. Feng, J. Yang, Z. Zhang, L. Liu, Y. Xia, D. Shen, *J. Alloy. Compd.* **2020**, *840*, 155585.
[20] C. Gao, Y. Wang, S. Fu, D. Xia, Y. Han, J. Ma, H. Xu, B. Li, A. Shen, Y. Liu, *ACS Appl. Mater. Interfaces* **2023**, *15*, 38612.
[21] Z. Li, Z. Feng, Y. Xu, Q. Feng, W. Zhu, D. Chen, H. Zhou, J. Zhang, C. Zhang, Y. Hao, *IEEE Trans. Electron. Dev.* **2022**, *69*, 1143.

[22] S. Hu, D. Han, K. Jiang, N. Liu, W. Wang, J. Zhang, K. Liu, T. Zhang, W. Zhang, J. Ye, *Appl. Phys. Express* **2023**, *16*, 021005.
[23] Y. Han, Y. Wang, D. Xia, S. Fu, C. Gao, J. Ma, H. Xu, B. Li, A. Shen, Y. Liu, *Small Methods* **2023**, *7*, 2300041.
[24] H.-S. Kim, S. H. Jeon, J. S. Park, T. S. Kim, K. S. Son, J.-B. Seon, S.-J. Seo, S.-J. Kim, E. Lee, J. G. Chung, H. Lee, S. Han, M. Ryu, S. Y. Lee, K. Kim, *Sci. Rep.* **2012**, *3*, 1459.
[25] Y. Wang, M. Kim, A. S. Chabungbam, D.-E. Kim, H.-H. Park, *Appl. Surf. Sci.* **2022**, *579*, 152170.
[26] Y. Liu, S. Wei, C. Shan, M. Zhao, S.-Y. Lien, M.-K. Lee, *J. Mater. Res. Technol.* **2022**, *21*, 3113.
[27] Y. F. Zhang, X. H. Chen, Y. Xu, H. H. Gong, Y. Yang, F. F. Ren, B. Liu, S. L. Gu, R. Zhang, D. J, A. C. S. A Ye, *Electron. Mater.* **2020**, *2*, 808.
[28] F. Xian, L. Xu, G. Zheng, Z. Cao, J. Li, S. Pei, J. Ye, *Appl. Phys. Lett.* **2019**, *115*, 231901.
[29] H.-P. Ma, X.-X. Li, J.-H. Yang, P. Cheng, W. Huang, J. Zhu, T.-C. Jen, Q. Guo, H.-L. Lu, D. W. Zhang, *Chem. Mater.* **2019**, *31*, 7405.
[30] H.-P. Ma, J.-H. Yang, J.-J. Tao, K.-P. Yuan, P.-H. Cheng, W. Huang, J.-C. Wang, Q.-X. Guo, H.-L. Lu, D. W. Zhang, *Nano Energy* **2019**, *66*, 104089.
[31] Z. Zhou, G. Liao, X. Song, Q. Dai, L. Sun, Y. Peng, P. Wang, *Nanoscale Res. Lett.* **2022**, *17*, 19.
[32] H. Yan, Y. Li, J.-K. Qin, B. Xu, P.-A. Hu, L. Zhen, C.-Y. Xu, *Small* **2021**, *17*, 2007739.
[33] Z. H. Xu, L. Tang, S. W. Zhang, J. Z. Li, B. L. Liu, S. C. Zhao, C. J. Yu, G. D. Wei, *Mater. Today Phys.* **2020**, *15*, 100273.
[34] T. L. Zhao, H. L. He, C. Wu, L. Lai, Y. X. Ma, H. Yang, H. Z. Hu, A. P. Liu, D. Y. Guo, S. L. Wang, A. C. S. Appl, *Nano Mater.* **2023**, *6*, 3856.
[35] X. Y. Liu, S. Y. Li, Z. Q. Li, F. Cao, L. Su, D. V. Shtansky, X. S. Fang, *ACS Appl. Mater. Interfaces* **2022**, *14*, 48936.
[36] H. Yoo, I. S. Lee, S. Jung, S. M. Rho, B. H. Kang, H. J. Kim, *Adv. Mater.* **2021**, *33*, 2006091.
[37] S. Jeon, S.-E. Ahn, I. Song, C. J. Kim, U.-I. Chung, E. Lee, I. Yoo, A. Nathan, S. Lee, K. Ghaffarzadeh, J. Robertson, K. Kim, *Nat. Mater.* **2012**, *11*, 301.
[38] L. Deng, H. Hu, Y. Wang, C. Wu, H. He, J. Li, X. Luo, F. Zhang, D. Guo, *Appl. Surf. Sci.* **2022**, *604*, 154459.
[39] T. Oshima, T. Okuno, S. Fujita, *Jpn. J. Appl. Phys.* **2007**, *46*, 7217e7220.
[40] C. Wu, D. Y. Guo, L. Y. Zhang, P. G. Li, F. B. Zhang, C. K. Tan, S. L. Wang, A. P. Liu, F. M. Wu, W. H. Tang, *Appl. Phys. Lett.* **2020**, *116*, 072102.
[41] Y. C. Chen, Y. J. Lu, X. Yang, S. F. Li, K. Y. Li, X. X. Chen, Z. Y. Xu, J. H. Zang, C. X. Shan, *Mater. Today Phys.* **2021**, *18*, 100369.
[42] Z. Liu, S. Li, Z. Yan, Y. Liu, Y. Zhi, X. Wang, Z. Wu, P. Li, W. Tang, *J. Mater. Chem. C* **2020**, *8*, 5071.
[43] J. Chen, J. Zhao, S. Feng, L. Zhang, Y. Cheng, H. Liao, Z. Zheng, X. Chen, Z. Gao, K. J. Chen, M. Hua, *Adv. Mater.* **2023**, *35*, 2208960.
[44] S. Cui, Z. Mei, Y. Zhang, H. Liang, X. Du, *Adv. Opt. Mater.* **2017**, *5*, 1700454.
[45] L.-X. Qian, Z.-H. Wu, Y.-Y. Zhang, P. T. Lai, X.-Z. Liu, Y.-R. Li, *ACS Photonics* **2017**, *4*, 2203.
[46] Z. Wu, L. Jiao, X. Wang, D. Guo, W. Li, L. Li, F. Huang, W. Tang, *J. Mater. Chem. C* **2017**, *5*, 8688.
[47] C. Wu, C. He, D. Guo, F. Zhang, P. Li, S. Wang, A. Liu, F. Wu, W. Tang, *Mater. Today Phys.* **2021**, *12*, 100193.
[48] J. Yu, M. Yu, Z. Wang, L. Yuan, Y. Huang, L. Zhang, Y. Zhang, R. Jia, *IEEE Trans. Electron. Dev.* **2020**, *67*, 3199.
[49] Y.-C. Chen, Y.-J. Lu, C.-N. Lin, Y.-Z. Tian, C.-J. Gao, L. Dong, C.-X. Shan, *J. Mater. Chem. C* **2018**, *6*, 5727.
[50] S. Li, Y. Zhi, C. Lu, C. Wu, Z. Yan, Z. Liu, J. Yang, X. Chu, D. Guo, P. Li, Z. Wu, W. Tang, *J. Phys. Chem. Lett.* **2021**, *12*, 447.
[51] R. Zhuo, D. Wu, Y. Wang, E. Wu, C. Jia, Z. Shi, T. Xu, Y. Tian, X. Li, *J. Mater. Chem. C* **2018**, *6*, 10982.
[52] H. Wang, H. Chen, L. Li, Y. Wang, L. Su, W. Bian, B. Li, X. Fang, *J. Phys. Chem. Lett.* **2019**, *10*, 6850.
[53] J. Zhang, S. Jiao, D. Wang, S. Gao, J. Wang, L. Zhao, *Appl. Surf. Sci.* **2021**, *541*, 148380.